Real-time chiral dynamics from a digital quantum simulation

Dmitri E. Kharzeev [1,2,3,*] and Yuta Kikuchi [3,†]

[1]*Department of Physics and Astronomy, Stony Brook University, Stony Brook, New York 11794-3800, USA*
[2]*Department of Physics, Brookhaven National Laboratory, Upton, New York 11973-5000, USA*
[3]*RIKEN-BNL Research Center, Brookhaven National Laboratory, Upton, New York 11973-5000, USA*

The chiral magnetic effect in a strong magnetic field can be described using the chiral anomaly in the $(1 + 1)$-dimensional massive Schwinger model with a time-dependent θ term. We perform a digital quantum simulation of the model at finite θ angle and vanishing gauge coupling using an IBM-Q digital quantum simulator, and observe the corresponding vector current induced in a system of relativistic fermions by a global *chiral quench*—a sudden change in the chiral chemical potential or θ angle. At finite fermion mass, there appears an additional contribution to this current that stems from the nonanomalous relaxation of chirality. Our results are relevant for the real-time dynamics of chiral magnetic effect in heavy ion collisions and in chiral materials, as well as for modeling high-energy processes at hadron colliders.

I. INTRODUCTION

Quantum theories possess a multidimensional Hilbert space that becomes very large for relativistic and/or many-body systems. This is why, in addressing the real-time dynamics, the use of quantum simulations potentially provides an exponential advantage over the classical simulations in terms of required computational time and memory [1,2]. Quantum simulations are also free from the sign problem that obstructs the use of Markov chain Monte Carlo methods. Because of this, along with the rapid development of digital and analog quantum computers, quantum simulations become a valuable source of information about the real-time behavior of relativistic and many-body systems [3–40].

The chiral magnetic effect (CME) is a generation of electric current in an external magnetic field induced by the chiral asymmetry between the right- and left-handed fermions [41]; see [42,43] for reviews and references. It is a nonequilibrium phenomenon stemming from the relaxation of chiral asymmetry via the chiral anomaly [44,45]. In high-energy heavy ion collisions, the CME can reveal topological fluctuations in QCD matter [46]. These fluctuations are akin to the electroweak sphalerons in the early universe that induce the baryon asymmetry. The experimental study of the effect is ongoing at the Relativistic Heavy Ion Collider at BNL and the Large Hadron Collider at CERN; see [47] for review. This effect can also be studied in three-dimensional chiral materials

(Dirac and Weyl semimetals) subjected to parallel electric and magnetic fields, and the CME has been observed in a Dirac semimetal $ZrTe_5$ [48] and other materials.

In a constant magnetic field and a given chiral chemical potential (the difference between the chemical potentials of the right- and left-handed fermions), the magnitude of the CME current is completely fixed by the chiral anomaly. However, this is not so for a time-dependent magnetic field [49], or for a time-dependent chiral chemical potential. One of the most important effects that determine the real-time dynamics of the CME is the chirality flipping—the transitions between the right- and left-handed fermions that are not related to the anomaly. The simplest mechanism producing such transitions arises from the finite masses of the fermions, since they induce nonconservation of the axial current. The mass effects are important for applications since the quarks in QCD are massive, and quasiparticles in many Dirac materials possess a finite gap.

In the limit of a strong magnetic field, the dynamics of chiral fermions becomes $(1 + 1)$-dimensional, since the fermions are frozen at the lowest Landau levels that are not degenerate in spin, and are thus chiral. Indeed, the real-time dynamics of CME and of the *chiral magnetic wave* can be described [50] within the $(1 + 1)$-dimensional QED, the Schwinger model [51]. The chiral anomaly relation in $(1 + 1)$ dimensions has the form

$$\partial_\mu J_5^\mu = \frac{1}{\pi} E + 2im\bar{\psi}\gamma_5\psi, \tag{1}$$

where $J_5^\mu = \bar{\psi}\gamma^\mu\gamma^5\psi$ is the axial current, E is electric field, and m is the fermion mass. The first term represents the chiral anomaly and the second one is due to nonconservation of chirality induced by the masses of the fermions. It is well known [52–54] that a background electric field E_{cl} in the

*dmitri.kharzeev@stonybrook.edu
†yuta.kikuchiATriken.jp

Schwinger model can be introduced through the θ angle:

$$E_{\text{cl}} = g\frac{\theta}{2\pi}. \qquad (2)$$

The real-time dynamics of CME can thus be studied in the Schwinger model by considering the time-dependent θ angle. While the CME stems from the anomaly term, it is very important for applications to understand the role of the second term in (1) in the relaxation of the vector current. This is the goal of our work.

To accomplish this goal, we need to separate the effect of the anomaly from the effect caused by the masses of the fermions in (1). This can be achieved by first applying the chiral rotation $\psi \to e^{i\gamma_5\theta/2}\psi$ with $\theta = \theta(t)$ to the fermion fields ψ, and then by putting the coupling constant g to zero. In this limit of the theory, the time variation in θ does not induce a background electric field [see (2)], but it does induce a chiral imbalance between the left- and right-handed fermions through the chiral chemical potential

$$\mu_5 = -\frac{\dot{\theta}}{2}. \qquad (3)$$

Since the term describing the nonanomalous chirality flipping in (1) vanishes at $m = 0$, in this limit of the theory the chiral chemical potential can induce the vector current only at finite fermion mass. In other words, a chirally imbalanced state with $\mu_5 \neq 0$ at $m = 0$ cannot relax to a state with $\mu_5 = 0$. This can be seen formally by observing that the Hamiltonian of the model in the chiral limit of $m = 0$ commutes with the vector current operator, even at $\mu_5 \neq 0$. This means that a chiral imbalance indeed cannot induce a vector current in the chiral limit of massless fermions.

The situation changes when the fermions become massive. In this case, a chirally imbalanced state can relax to the true ground state with $\mu_5 = 0$, and generate a vector current during this relaxation process. It is clear that this is a real-time phenomenon, and we need to introduce a time-dependent chiral perturbation to study it. We will do this by subjecting the system to two different types of global (spatially independent) *chiral quenches*.

(1) Prepare the system in the state with $\theta = 0$ at times $t < 0$. Then, starting at $t = 0$, rotate the θ angle according to $\theta = -2\mu_5 t$, corresponding to a constant chiral chemical potential (3).

(2) As before, prepare the system in the state with $\theta = 0$ at times $t < 0$. Then abruptly change the θ angle at $t = 0$ to a finite constant value corresponding to $\mu_5 = 0$; see [55] for an earlier study of this quench type.

We will refer to these two global quench protocols as the μ_5 *quench* and the θ *quench*, respectively.

II. FREE FERMION MODEL AT FINITE θ ANGLE

We choose the following basis for the gamma matrices:

$$\gamma_0 = Z, \quad \gamma_1 = -iY, \quad \gamma_5 = \gamma_0\gamma_1 = -X, \qquad (4)$$

where $X \equiv \sigma_x$, $Y \equiv \sigma_y$, and $Z \equiv \sigma_z$ are the Pauli matrices.

The action of the massive Schwinger model with θ term in $(1 + 1)$-dimensional Minkowski space is

$$S = \int d^2x \left[-\frac{1}{4}F^{\mu\nu}F_{\mu\nu} + \frac{g\theta}{4\pi}\epsilon^{\mu\nu}F_{\mu\nu} + \bar{\psi}(i\gamma^\mu D_\mu - m)\psi \right], \qquad (5)$$

with $D_\mu = \partial_\mu - igA_\mu$. Note that the gauge field A_μ and the coupling constant g have mass dimensions 0 and 1, respectively. In what follows, we fix the gauge by putting $A_0 = 0$. From the action (5) the canonical momentum conjugate to A_1 can be read off as $\Pi = \dot{A}_1 - \frac{g\theta}{2\pi}$. The corresponding Hamiltonian is then given by

$$H = \int dx \left[\frac{1}{2}\left(\Pi + \frac{g\theta}{2\pi}\right)^2 + \bar{\psi}(i\gamma_1 D_1 + m)\psi \right], \qquad (6)$$

with commutation relations $[A_1(x), \Pi(y)] = i\delta(x - y)$ and $\{\psi(x), \bar{\psi}(y)\} = \gamma_0\delta(x - y)$. Therefore, the term $g\theta/2\pi$ can be identified with a classical contribution to the total electric field $E = \dot{A}_1$ [in agreement with (2)], while Π is the quantum contribution.

Upon the chiral transformation $\psi \to e^{i\gamma_5\theta/2}\psi$ and $\bar{\psi} \to \bar{\psi}e^{i\gamma_5\theta/2}$, the θ term is absorbed into the phase of the fermion mass term,

$$S = \int d^2x \left[-\frac{1}{4}F^{\mu\nu}F_{\mu\nu} + \bar{\psi}\left(i\gamma^\mu D_\mu + \frac{\dot{\theta}}{2}\gamma_0\gamma_5 - m\,e^{i\gamma_5\theta}\right)\psi \right], \qquad (7)$$

where $\theta = \theta(t)$ is a time-dependent parameter. We then decouple the gauge dynamics by taking the $g \to 0$ limit to study the free fermionic theory with chiral chemical potential $\mu_5 = -\dot{\theta}/2$ and chirally rotated mass term. The resulting Hamiltonian is given by

$$H = \int dx\,\bar{\psi}\left[\gamma_1\left(i\partial_1 - \frac{\dot{\theta}}{2}\right) + m\,e^{i\gamma_5\theta}\right]\psi. \qquad (8)$$

Let us consider how the vector current is induced as a result of the chiral quench. In our $(1+1)$-dimensional system, the axial charge density $q_5(x) \equiv \bar{\psi}\gamma_5\gamma_0\psi(x)$ and the vector current density $j(x) \equiv \bar{\psi}\gamma_1\psi(x)$ are related by $q_5 = -j$; the vector charge density $q(x) \equiv \bar{\psi}\gamma_0\psi(x)$ and axial current density $j_5(x) \equiv \bar{\psi}\gamma_5\gamma_1\psi(x)$ are identical, $q = j_5$. The Hamiltonian before the quench H_0 is obtained from (8) by setting $\theta = 0$ and $\dot{\theta} = -2\mu_5 = 0$. The full Hamiltonian after the quench is

$$H = H_0 + \mu_5 J + m\bar{\psi}(e^{i\gamma_5\theta} - 1)\psi, \qquad (9)$$

with $J = \int dx\,j(x)$. The vector current is zero in the ground state before the quench ($t < 0$),

$$\langle J \rangle_0 = 0, \qquad (10)$$

where the expectation value $\langle \ldots \rangle_0$ is taken with respect to the ground state of H_0. In the massless case, the vector current is identically zero both before and after the quench,

$$\langle \bar{\mathcal{T}}[e^{i\int_0^t dt\,H}]J\,\mathcal{T}[e^{-i\int_0^t dt\,H}]\rangle_0 = 0, \qquad (11)$$

because H_0 and H both commute with $J = -Q_5$. $\mathcal{T}$ ($\bar{\mathcal{T}}$) indicates that the operator product is (anti)time ordered. With

the fermion mass term included, H and J no longer commute,

$$[H, J] = 2m \cos\theta \int dx\, \bar{\psi}\gamma_5\psi(x) + 2im \sin\theta \int dx\, \bar{\psi}\psi(x). \tag{12}$$

Hence the current can take a finite value. Indeed, the current does not vanish and at short times behaves as (Appendix B)

$$\langle \bar{\mathcal{T}}[e^{i\int_0^{t'} dt\, H}] J\, \mathcal{T}[e^{-i\int_0^{t'} dt\, H}]\rangle_0$$

$$= i\int_0^t dt_1 \langle[H(t_1), J]\rangle_0 - \int_0^t dt_1 \int_0^{t_1} dt_2 \langle[H(t_2), [H(t_1), J]]\rangle_0$$

$$+ \mathcal{O}(t^3)$$

$$= \left(-2m\int_0^t dt_1 \sin\theta(t_1) - 2m\int_0^t dt_1 \int_0^{t_1} dt_2\, \dot{\theta}(t_2)\cos\theta(t_1)\right)$$

$$\times \int dx \langle\bar{\psi}\psi\rangle_0 - 4m\int_0^t dt_1 \int_0^{t_1} dt_2 \sin\theta(t_1)$$

$$\times \int dx \langle\bar{\psi}\gamma_5\partial_1\psi\rangle_0 + \mathcal{O}(t^3). \tag{13}$$

Spin Hamiltonian of the lattice fermion model

Let us now set up this problem in the lattice form suitable for a digital quantum simulation. We impose a periodic boundary condition, where the zeroth and Nth sites are identified and N is an even integer. The staggered Hamiltonian is [56,57]

$$H = -iw\sum_{n=0}^{N-1}[\chi_n^\dagger\chi_{n+1} - \chi_{n+1}^\dagger\chi_n]$$

$$- \frac{\dot{\theta}}{4}\sum_{n=1}^{N-1}[\chi_n^\dagger\chi_{n+1} + \chi_{n+1}^\dagger\chi_n]$$

$$+ m\cos\theta\sum_{n=0}^{N-1}(-1)^n\chi_n^\dagger\chi_n$$

$$+ i\frac{m}{2}\sin\theta\sum_{n=0}^{N-1}(-1)^n[\chi_n^\dagger\chi_{n+1} - \chi_{n+1}^\dagger\chi_n], \tag{14}$$

where a is the lattice spacing and $w = (2a)^{-1}$ (see Appendix A for details). For the purpose of quantum simulation, we apply the Jordan-Wigner transformation [58],

$$\chi_n = \frac{X_n - iY_n}{2}\prod_{i=0}^{n-1}(-iZ_i), \quad \chi_n^\dagger = \frac{X_n + iY_n}{2}\prod_{i=0}^{n-1}iZ_i, \tag{15}$$

which leads to the desired spin Hamiltonian:

$$H = H_1 + H_2 + H_3 + H_4 + H_5,$$

$$H_1 = \frac{1}{2}\sum_{n=0}^{\frac{N}{2}-1}\left(w - \frac{m}{2}(-1)^n\sin\theta\right)[X_{2n}X_{2n+1} + Y_{2n}Y_{2n+1}],$$

$$H_2 = \frac{1}{2}\sum_{n=1}^{\frac{N}{2}-1}\left(w - \frac{m}{2}(-1)^n\sin\theta\right)[X_{2n-1}X_{2n} + Y_{2n-1}Y_{2n}]$$

$$+ \frac{(-1)^{\frac{N}{2}}}{2}\left(w - \frac{m}{2}(-1)^{N-1}\sin\theta\right)$$

$$\times [X_{N-1}X_0 + Y_{N-1}Y_0]\prod_{i=1}^{N-2}Z_i,$$

$$H_3 = -\frac{\dot{\theta}}{8}\sum_{n=0}^{\frac{N}{2}-1}[X_{2n}Y_{2n+1} - Y_{2n}X_{2n+1}],$$

$$H_4 = -\frac{\dot{\theta}}{8}\sum_{n=1}^{\frac{N}{2}-1}[X_{2n-1}Y_{2n} - Y_{2n-1}X_{2n}]$$

$$- \frac{(-1)^{\frac{N}{2}}\dot{\theta}}{8}[X_{N-1}Y_0 - Y_{N-1}X_0]\prod_{i=1}^{N-2}Z_i,$$

$$H_5 = \frac{m\cos\theta}{2}\sum_{n=0}^{N-1}(-1)^n Z_n. \tag{16}$$

It should be stressed that each H_i does not violate the particle number conservation. This decomposition enables us to carry out the Suzuki-Trotter decomposition (19) with the particle number conservation preserved exactly.

We are interested in computing the spatial average of vector current, which, in terms of spin operators, is expressed as

$$\bar{J} = \bar{J}_1 + \bar{J}_2,$$

$$\bar{J}_1 = \frac{w}{2N}\sum_{n=0}^{\frac{N}{2}-1}(X_{2n}Y_{2n+1} - Y_{2n}X_{2n+1}),$$

$$\bar{J}_2 = \frac{w}{2N}\sum_{n=1}^{\frac{N}{2}-1}(X_{2n-1}Y_{2n} - Y_{2n-1}X_{2n})$$

$$+ \frac{(-1)^{\frac{N}{2}}w}{2N}(X_{N-1}Y_0 - Y_{N-1}X_0)\prod_{i=1}^{N-2}Z_i. \tag{17}$$

We note that the relations (12) and (13) hold for corresponding operators defined on the lattice without taking a continuum limit.

III. REAL-TIME SIMULATION

We implement the quantum simulation for the global chiral quench using a IBM Q digital quantum simulator in the three following steps: initial state preparation, real-time evolution, and measurement.

A. Initial state preparation

We prepare the ground state, $|\Psi(0)\rangle$, of the Hamiltonian (16) at $\theta = 0$ and $\dot{\theta} = 0$ using a python package for exact diagonalization, QuSpin [59].[1] This state is used as the initial state in our studies of real-time chiral dynamics.

B. Time evolution with the Hamiltonian at $\theta \neq 0$

The time-evolution operator is applied to the initial state,

$$|\Psi(t)\rangle = \mathcal{T}[e^{-i \int_0^t dt' H(t')}]|\Psi(0)\rangle. \qquad (18)$$

We employ the trapezoidal discretization of integration and the Suzuki-Trotter decomposition in order to approximate the time-evolution operator, $\mathcal{T}[e^{-i \int_0^t dt' H(t')}]$, by elementary unitary gates. Applying the trapezoidal rule we approximate the integral by the sum, $\sum_{s=0}^{S} \tilde{H}^s := [H(0) + H(t)]/2 + \sum_{s=1}^{S-1} H(st/S) = \int_0^t dt' H(t') + \mathcal{O}(t^2/S^2)$. Then, the Suzuki-Trotter decomposition is done as follows:

$$\prod_{s=0}^{S} e^{-i(\tilde{H}_5^s + \tilde{H}_4^s + \tilde{H}_3^s + \tilde{H}_2^s + \tilde{H}_1^s)\frac{t}{S}}$$

$$= e^{i\tilde{H}_2^{S+1}\frac{t}{2S}} \prod_{s=0}^{S} \left(e^{-i(\tilde{H}_2^{s+1} + \tilde{H}_2^s)\frac{t}{2S}} e^{-i\tilde{H}_1^s \frac{t}{2S}} e^{-i\tilde{H}_3^s \frac{t}{2S}} e^{-i\tilde{H}_5^s \frac{t}{2S}} \right.$$

$$\left. \times e^{-i\tilde{H}_4^s \frac{t}{S}} e^{-i\tilde{H}_5^s \frac{t}{2S}} e^{-i\tilde{H}_3^s \frac{t}{2S}} e^{-i\tilde{H}_1^s \frac{t}{2S}} \right) e^{-i\tilde{H}_2^0 \frac{t}{2S}} + \mathcal{O}(t^3/S^2), \qquad (19)$$

where $\tilde{H}_i^s := \tilde{H}_i(st/S)$. The operator product is understood to be time ordered. Hence the total decomposition error is $\mathcal{O}(t^3/S^2)$, which we call the Trotter error. The circuit implementation of each unitary is given in Appendix C.

Here, we consider two protocols for the quench described in Sec. I.

(1) μ_5 quench: at $t = 0$ we abruptly turn on the chiral chemical potential μ_5 and keep it constant during the subsequent evolution.

(2) θ quench: at $t = 0$ we abruptly change the value of the θ angle, that introduces the pulse in the chiral chemical potential $-\frac{\dot{\theta}}{2}\delta(t)$.

The unitary evolution with the use of the Suzuki-Trotter decomposition may be interpreted as the Hamiltonian evolution with the shadow Hamiltonian H_{sh}, defined by

$$e^{-iH_{\text{sh}}t} := e^{i\tilde{H}_2^{S+1}\frac{t}{2S}} \prod_{s=0}^{S} \left(e^{-i(\tilde{H}_2^{s+1} + \tilde{H}_2^s)\frac{t}{2S}} e^{-i\tilde{H}_1^s \frac{t}{2S}} e^{-i\tilde{H}_3^s \frac{t}{2S}} \right.$$

$$\left. \times e^{-i\tilde{H}_5^s \frac{t}{2S}} e^{-i\tilde{H}_4^s \frac{t}{S}} e^{-i\tilde{H}_5^s \frac{t}{2S}} e^{-i\tilde{H}_3^s \frac{t}{2S}} e^{-i\tilde{H}_1^s \frac{t}{2S}} \right) e^{-i\tilde{H}_2^0 \frac{t}{2S}}. \qquad (20)$$

The shadow Hamiltonian H_{sh} differs from the original Hamiltonian (16) by the Trotter error. Since we use the exact ground state of (16) as an initial state, the Hamiltonian evolution H_{sh} introduces an additional quench due to the Trotter error in addition to the μ_5 or θ quench. This artificial quench accounts

---

[1] Adiabatic state preparation of the massive Schwinger model at finite θ angle was studied in detail in [40] by carefully taking thermodynamic and continuum limits of the lattice Schwinger model.
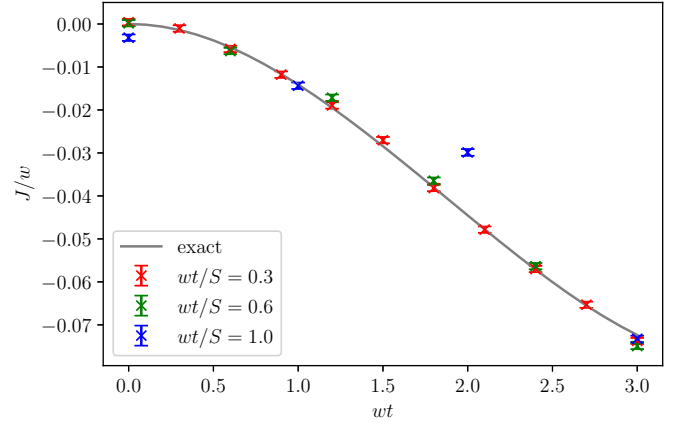

FIG. 1. t/S dependence of the vector current following the μ_5 quench, with lattice size $N = 12$, fermion mass $M = 0.1w$, and chiral chemical potential $\mu_5 = 0.2w$. The error bar for each data point represents the statistical error which is estimated by performing 100 000 measurements. The solid lines are exact results. The discretization error becomes significant for $wt/S = 1.0$.

for a small oscillation of $\mathcal{O}(t^3/S^2)$ in the physical quantities such as vector current as shown in Fig. 1.

C. Evaluation of the vector current

Having obtained the $|\Psi(t)\rangle$ at time t, we evaluate the expectation value of the vector current density $\langle \bar{J} \rangle := \langle \Psi(t)|\bar{J}|\Psi(t)\rangle$, where $\bar{J}$ is given by (17). Since the operators $\bar{J}_1$ and $\bar{J}_2$ do not commute with each other, we carry out two independent measurements to read off the expectation value of $\bar{J}$.

Let us first find a way to calculate $\langle \bar{J}_1 \rangle$. We note the following identities:

$$(HS^\dagger)_i CX_{ij}(X_i Y_j) CX_{ij}(SH)_i = Z_i Z_j,$$
$$(HS^\dagger)_i CX_{ij}(Y_i X_j) CX_{ij}(SH)_i = Z_i I_j, \qquad (21)$$

where H_i and S_i are Hadamard and $\pi/4$ gates acting on the ith qubit. CX_{ij} is a controlled-NOT (CNOT) gate with the ith and jth qubits being control and target qubits, respectively. These identities imply that the Z_i and Z_j measurements on a state $(SH)_i CX_{ij}|\psi\rangle$ yield the data needed to compute $\langle X_i Y_j \rangle$ and $\langle Y_i X_j \rangle$. The measurement is performed by the following circuit:

$$(22)$$

Given the counts of the digits (d_i, d_j) from the above measurements, we can extract the operator expectation values,

$$\langle X_i Y_j \rangle = \sum_{(d_i, d_j)} (1 - 2d_i)(1 - 2d_j) \frac{\text{counts}_{d_i, d_j}}{\text{shots}},$$

$$\langle Y_i X_j \rangle = \sum_{(d_i, d_j)} (1 - 2d_i) \frac{\text{counts}_{d_i, d_j}}{\text{shots}}, \qquad (23)$$
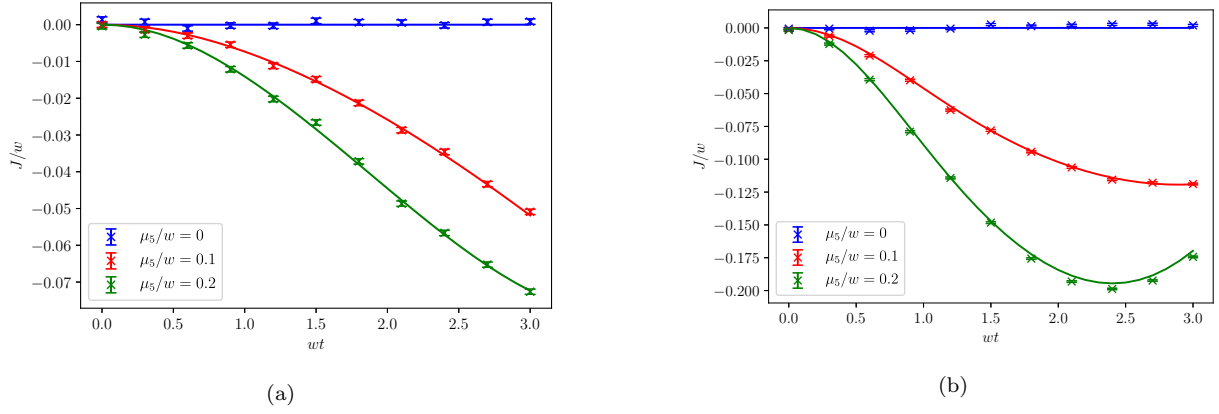
which allows us to compute $\langle \bar{J}_1 \rangle$.

FIG. 2. Vector current densities after the μ_5 quench with lattice size $N = 12$ and temporal lattice spacing $wt/S = 0.3$. The fermion mass is set to be (a) $M = 0.1w$ and (b) $M = 0.5w$. The error bar for each data point represents the statistical errors which are estimated by performing 100 000 measurements. The solid lines are exact results.

The same argument applies to $\bar{J}_2$ except for the operators $X_{N-1}Y_0 \prod_{i=1}^{N-2} Z_i$ and $Y_{N-1}X_0 \prod_{i=1}^{N-2} Z_i$. We use the identities

$$
\left(\prod_{n=1}^{\frac{N}{2}} (HS^\dagger)_{2n-1} CX_{2n-1,2n} \right) \left(X_{N-1}Y_0 \prod_{i=1}^{N-2} Z_i \right)
$$
$$
\times \left(\prod_{m=1}^{\frac{N}{2}} CX_{2m-1,2m} (SH)_{2n-1} \right) = Z_0 \left(\prod_{i=1}^{\frac{N}{2}-1} Z_{2i} \right) Z_{N-1},
$$
$$
\left(\prod_{n=1}^{\frac{N}{2}} (HS^\dagger)_{2n-1} CX_{2n-1,2n} \right) \left(Y_{N-1}X_0 \prod_{i=1}^{N-2} Z_i \right)
$$
$$
\times \left(\prod_{m=1}^{\frac{N}{2}} CX_{2m-1,2m} (SH)_{2n-1} \right) = I_0 \left(\prod_{i=1}^{\frac{N}{2}-1} Z_{2i} \right) Z_{N-1},
$$

(24)

where the Nth site is identified with the zeroth site. Therefore, provided the counts of the digit $(d_0, \ldots, d_{N-1})$, we can extract the operator expectation values,

$$
\left\langle X_{N-1}Y_0 \prod_{i=1}^{N-2} Z_i \right\rangle = \sum_{(d_0,\ldots,d_{N-1})} \left(\prod_{i=0}^{\frac{N}{2}-1} (1 - 2d_{2i}) \right) (1 - 2d_{N-1})
$$
$$
\times \frac{\text{counts}_{d_0,\ldots,d_{N-1}}}{\text{shots}},
$$
$$
\left\langle Y_{N-1}X_0 \prod_{i=1}^{N-2} Z_i \right\rangle = \sum_{(d_0,\ldots,d_{N-1})} \left(\prod_{i=1}^{\frac{N}{2}-1} (1 - 2d_{2i}) \right) (1 - 2d_{N-1})
$$
$$
\times \frac{\text{counts}_{d_0,\ldots,d_{N-1}}}{\text{shots}}.
$$

(25)

These, combined with (23), provide all the ingredients required to compute $\langle \bar{J}_2 \rangle$.

IV. RESULTS AND DISCUSSION

Let us begin by discussing the features of our results at short time after the μ_5 quench, where $\theta = -2\mu_5 t$.

(1) The expectation value of the vector current at short times (13) is given by

$$
\langle \bar{J} \rangle = 4\mu_5 m t^2 \langle \bar{\psi}\psi \rangle_{\text{ave}} + \mathcal{O}(t^3) \approx -c\mu_5 m^2 t^2, \quad (26)
$$

where $\langle \bar{\psi}\psi \rangle_{\text{ave}}$ is the spatial average of the scalar condensate (proportional to $-m$) and c is a constant. The above expression for $\langle \bar{J} \rangle$ exhibits an approximately quadratic dependence on time after the quench, which agrees with the behavior seen in Figs. 2.

(2) The vector current is also approximately quadratic in the fermion mass m and linear in the chiral chemical potential μ_5, as expected from (26). The explicit comparison between the data and the short-time behavior (26) is shown in Appendix B.

Our quantum simulation results are in good agreement with the results based on exact diagonalization as shown in Figs. 2 and 3. Note that the error bars account for the statistical error but not the Trotter error, that results in deviation from the exact result as explained at the end of Sec. III B. At larger times, the vector current exhibits a rich dynamics with nonlinear dependence on time. Some features of this dynamics can still be understood qualitatively. For the μ_5 quench, the current tends to a finite value at late times (see Fig. 2), and then, at larger value of the mass, starts to exhibit saturation caused by the relaxation of chirality [see Fig. 2(b)]. For the θ quench, the current after the initial pulse at $t = 0$ relaxes back to zero (see Fig. 3), possibly with subsequent oscillations. This relaxation is faster for a larger value of the fermion mass, in accord with (1). For larger fermion masses, we observe the oscillation; for smaller masses, the oscillations, if present, are characterized by a larger period.

The real-time dynamics following the θ quench was extensively studied in [55] using exact diagonalization. The μ_5 quench that we investigated here is directly relevant for the real-time dynamics of the chiral magnetic effect.
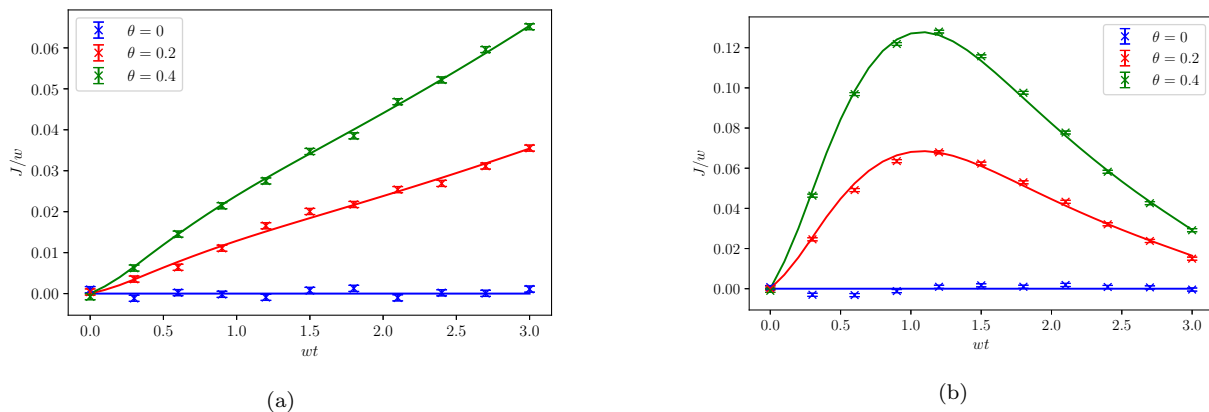
(a)

(b)

FIG. 3. Vector currents after the θ quench with lattice size $N = 12$ and temporal lattice spacing $wt/S = 0.3$. The fermion mass is set to be (a) $M = 0.1w$ and (b) $M = 0.5w$. The error bar for each data point represents the statistical errors which are estimated by performing 100 000 measurements. The solid lines are exact results.

V. SUMMARY AND OUTLOOK

We have considered the behavior of a free model of relativistic fermions under the global *chiral quenches* that abruptly change the value of the θ angle. It has been observed here that such quenches induce vector currents stemming from the dynamics of chirality relaxation. The resulting real-time dynamics of the vector current appears unexpectedly rich, and is determined by the interplay between the processes of chirality pumping induced by the rotating θ angle and chirality absorption and relaxation.

This pilot study clarifies the effect of explicit breaking of chiral symmetry by fermion mass on the real-time dynamics of the chiral magnetic effect. The computation that we have performed is amenable to a study using a classical computer; however, we feel that it is important to demonstrate the potential of quantum computation for describing the real-time dynamics of quantum field theories. The study of the effect of fermion mass on real-time chiral dynamics is relevant for many practical applications—e.g., the quarks in QCD, or chiral quasiparticles with a finite gap in Dirac semimetals. In addition, the Schwinger model has been used to model the fragmentation of quarks in high-energy collisions [56,60–65], and the relaxation of chirality is key to the dynamics of this process. Our results show how the fermion mass affects the relaxation to a steady state, and the behavior of the vector current.

In the future, we plan to include the dynamical gauge field to investigate the interplay of anomalous and mass-induced chirality relaxation in the generation of the chiral magnetic current. This will require developing a method for truncating the $U(1)$ gauge field. For example, if $U(1)$ is approximated by $\mathbb{Z}_N$, then in general per each site one needs $\log N$ qubits. However, in the Schwinger model, the absence of propagating gauge field modes allows one to use $\log N$ qubits per entire lattice. This should allow one to simulate the model with a moderate number of qubits.

ACKNOWLEDGMENTS

APPENDIX A: RELATION AMONG DIRAC FERMION, STAGGERED FERMION, AND SPIN OPERATORS

Given a theory with two-component Dirac fermion $\psi(x) = [\rho(x), \eta(x)]^{\mathrm{t}}$ defined on a continuum space-time, we place the theory on a spatial lattice by placing a one-component staggered fermion χ_n on each site. Letting lattice size be an even integer N and lattice space be a, $\chi_{2m}/\sqrt{a}$ is identified with $\rho(x = m)$ and $\chi_{2m+1}/\sqrt{a}$ is identified with $\eta(x = m)$, where m runs from zero to $N/2$. With this correspondence in mind, the following operators are translated from Dirac fermion to staggered fermion as follows:

$$\int dx \, \bar{\psi}\psi \leftrightarrow \sum_n (-1)^n \chi_n^\dagger \chi_n, \tag{A1}$$

$$\int dx \, \bar{\psi}\gamma_0\psi \leftrightarrow \sum_n \chi_n^\dagger \chi_n, \tag{A2}$$

$$\int dx \, \bar{\psi}\gamma_1\psi \leftrightarrow -\frac{1}{2}\sum_n [\chi_n^\dagger \chi_{n+1} + \chi_{n+1}^\dagger \chi_n], \tag{A3}$$

$$\int dx \, \bar{\psi}\gamma_5\psi \leftrightarrow -\frac{1}{2}\sum_n (-1)^n [\chi_n^\dagger \chi_{n+1} - \chi_{n+1}^\dagger \chi_n], \tag{A4}$$

$$\int dx \, \bar{\psi}\gamma_1\partial_1\psi \leftrightarrow -\frac{1}{2a}\sum_n [\chi_n^\dagger \chi_{n+1} - \chi_{n+1}^\dagger \chi_n]. \tag{A5}$$

The left-hand sides correctly reproduce the right-hand sides in the continuum limit $a \to 0$. The operators written in terms of staggered fermions are further converted to spin operators by using the Jordan-Wigner transformation (15).

We summarize the relation of operators among these representations:

Dirac	Staggered	Spin	
$\bar{\psi}\psi$	$\frac{(-1)^n}{a}\chi_n^\dagger\chi_n$	$\frac{(-1)^n}{2a}Z_n$	
$\bar{\psi}\gamma_0\psi$	$\frac{1}{a}\chi_n^\dagger\chi_n$	$\frac{1}{2a}Z_n$	
$\bar{\psi}\gamma_1\psi$	$\frac{1}{2a}\left[\chi_n^\dagger\chi_{n+1}+\chi_{n+1}^\dagger\chi_n\right]$	$\frac{1}{4a}\left[X_nY_{n+1}-X_nY_{n+1}\right]$	(A6)
$\bar{\psi}\gamma_5\psi$	$\frac{(-1)^n}{2a}\left[\chi_n^\dagger\chi_{n+1}-\chi_{n+1}^\dagger\chi_n\right]$	$-\frac{i(-1)^n}{4a}\left[X_nX_{n+1}+Y_nY_{n+1}\right]$	
$\bar{\psi}\gamma_1\partial_1\psi$	$-\frac{1}{2a^2}\left[\chi_n^\dagger\chi_{n+1}-\chi_{n+1}^\dagger\chi_n\right]$	$-\frac{i}{4a^2}\left[X_nX_{n+1}+Y_nY_{n+1}\right]$	

The expressions in each row are different representations of the same operators. More precisely, the operators in terms of staggered fermions and spins are equivalent up to constant terms and they agree with the operators of Dirac fermions in the continuum limit. Note that for $n = N - 1$ the operator $(-1)^{\frac{N}{2}+1}\prod_{i=1}^{N-2}Z_i$ has to be inserted in the spin representation in order to take account of the periodic boundary condition.

APPENDIX B: CURRENT AT SHORT TIME

The vector current at shot time is given by

$$\langle\bar{\mathcal{T}}[e^{i\int_0^t dt'H}]J\,\mathcal{T}[e^{-i\int_0^t dt'H}]\rangle_0$$
$$= i\int_0^t dt_1\langle[H(t_1),J]\rangle_0$$
$$- \int_0^t dt_1\int_0^{t_1} dt_2\langle[H(t_2),[H(t_1),J]]\rangle_0 + \mathcal{O}(t^3). \quad (B1)$$

The commutators are calculated as

$$[H(t_1),J] = \int dx\,dy[m\,\cos\theta(t_1)\bar{\psi}\psi(x)$$
$$+ im\,\sin\theta(t_1)\bar{\psi}\gamma_5\psi(x),\,\bar{\psi}\gamma_1\psi(y)]$$
$$= \int dx[2m\,\cos\theta(t_1)\bar{\psi}\gamma_5\psi + 2im\,\sin\theta(t_1)\bar{\psi}\psi], \quad (B2)$$

$$[H(t_2),[H(t_1),J]]$$
$$= \int dx\,dy\left[i\bar{\psi}\gamma_1\partial_1\psi(x) - \frac{\dot{\theta}(t_2)}{2}\bar{\psi}\gamma_1\psi(x)\right.$$
$$+ m\,\cos\theta(t_2)\bar{\psi}\psi(x) + im\,\sin\theta(t_2)\bar{\psi}\gamma_5\psi(x),$$
$$\left.2m\,\cos\theta(t_1)\bar{\psi}\gamma_5\psi(y) + 2im\,\sin\theta(t_1)\bar{\psi}\psi(y)\right]$$
$$= \int dx[-4im\,\cos\theta(t_1)\bar{\psi}\partial_1\psi + 4m\,\sin\theta(t_1)\bar{\psi}\gamma_5\partial_1\psi$$
$$+ 2m\dot{\theta}(t_2)\cos\theta(t_1)\bar{\psi}\psi + 2im\dot{\theta}(t_2)\sin\theta(t_1)\bar{\psi}\gamma_5\psi$$
$$+ 4m^2\bar{\psi}\gamma_1\psi]. \quad (B3)$$

Since the vacuum before the quench is parity symmetric,

$$\langle\bar{\psi}\gamma_5\psi\rangle_0 = 0, \quad \langle\bar{\psi}\gamma_1\psi\rangle_0 = 0, \quad \langle\bar{\psi}\partial_1\psi\rangle_0 = 0. \quad (B4)$$

Hence the current is computed as

$$\langle\bar{\mathcal{T}}[e^{i\int_0^t dt'H}]J\,\mathcal{T}[e^{-i\int_0^t dt'H}]\rangle_0$$
$$= \left(-2m\int_0^t dt_1\sin\theta(t_1)\right.$$
$$\left.- 2m\int_0^t dt_1\int_0^{t_1} dt_2\dot{\theta}(t_2)\cos\theta(t_1)\right)\int dx\langle\bar{\psi}\psi\rangle_0$$
$$- 4m\int_0^t dt_1\int_0^{t_1} dt_2\sin\theta(t_1)\int dx\langle\bar{\psi}\gamma_5\partial_1\psi\rangle_0 + \mathcal{O}(t^3). \quad (B5)$$

In case of the μ_5 quench, where $\theta = -2\mu_5 t$, it is further simplified to

$$\langle\bar{\mathcal{T}}[e^{i\int_0^t dt'H}]J\,\mathcal{T}[e^{-i\int_0^t dt'H}]\rangle_0 = 4m\mu_5 t^2\int dx\langle\bar{\psi}\psi\rangle_0 + \mathcal{O}(t^3). \quad (B6)$$
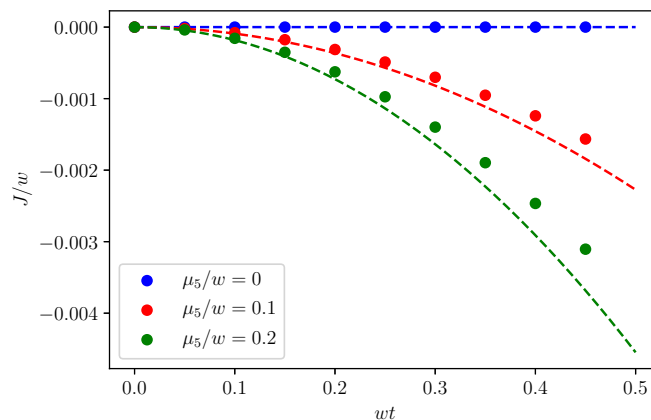
The short-time behavior is shown in Fig. 4.

FIG. 4. Short-time behavior of the vector current following the θ quench with lattice size $N = 12$ and fermion mass $M = 0.1w$. The data points are obtained by exact diagonalization and dashed lines are short-time behavior of the current (B6).

APPENDIX C: QUANTUM CIRCUITS FOR TIME EVOLUTION

We show the circuit implementations used for time-evolution operator (19):

$$e^{-i\alpha Z_i Z_j} =$$

$$(\text{C1})$$

where $R_Z(\theta) := e^{-i\frac{\theta}{2}Z}$,

$$e^{-i\alpha(X_i X_j + Y_i Y_j)} =$$

$$(\text{C2})$$

Then, $e^{-i\alpha(XY-YX)}$ is immediately implemented by noting

$$e^{-i\alpha(X_i Y_j - Y_i X_j)} = S_j e^{-i\alpha(X_i X_j + Y_i Y_j)} S_j^\dagger. \qquad (\text{C3})$$

The evolution operator involving a nonlocal term is implemented by the following circuit:

$$e^{-i\alpha(X_0 X_{N-1} + Y_0 Y_{N-1}) \prod_{i=1}^{N-2} Z_i} =$$

$$(\text{C4})$$

Then, $e^{-i\alpha(XY-YX)}$ is immediately implemented by noting

$$e^{-i\alpha(X_0 Y_{N-1} - Y_0 X_{N-1}) \prod_{i=1}^{N-2} Z_i} = S_{N-1} e^{-i\alpha(X_0 X_{N-1} + Y_0 Y_{N-1}) \prod_{i=1}^{N-2} Z_i} S_{N-1}^\dagger. \qquad (\text{C5})$$

[1] R. P. Feynman, Simulating physics with computers, Int. J. Theor. Phys. **21**, 467 (1982).

[2] S. Lloyd, Universal quantum simulators, Science **273**, 1073 (1996).

[3] A. Wallraff, D. I. Schuster, A. Blais, L. Frunzio, R. S. Huang, J. Majer, S. Kumar, S. M. Girvin, and R. J. Schoelkopf, Strong coupling of a single photon to a superconducting qubit using circuit quantum electrodynamics, Nature (London) **431**, 162 (2004).

[4] J. Majer, J. M. Chow, J. M. Gambetta, J. Koch, B. R. Johnson, J. A. Schreier, L. Frunzio, D. I. Schuster, A. A. Houck, A. Wallraff, A. Blais, M. H. Devoret, S. M. Girvin, and R. J. Schoelkopf, Coupling superconducting qubits via a cavity bus, Nature (London) **449**, 443 (2007).

[5] S. P. Jordan, K. S. M. Lee, and J. Preskill, Quantum algorithms for quantum field theories, Science **336**, 1130 (2012).

[6] S. P. Jordan, K. S. M. Lee, and J. Preskill, Quantum computation of scattering in scalar quantum field theories, Quantum Inf. Comput. **14**, 1014 (2014).

[7] E. Zohar, J. I. Cirac, and B. Reznik, Simulating Compact Quantum Electrodynamics with Ultracold Atoms: Probing Confinement and Nonperturbative Effects, Phys. Rev. Lett. **109**, 125302 (2012).

[8] E. Zohar, J. I. Cirac, and B. Reznik, Cold-Atom Quantum Simulator for SU(2) Yang-Mills Lattice Gauge Theory, Phys. Rev. Lett. **110**, 125304 (2013).

[9] D. Banerjee, M. Bögli, M. Dalmonte, E. Rico, P. Stebler, U. J. Wiese, and P. Zoller, Atomic Quantum Simulation of U(N) and SU(N) Non-Abelian Lattice Gauge Theories, Phys. Rev. Lett. **110**, 125303 (2013).

[10] D. Banerjee, M. Dalmonte, M. Muller, E. Rico, P. Stebler, U. J. Wiese, and P. Zoller, Atomic Quantum Simulation of Dynamical Gauge Fields coupled to Fermionic Matter: From String Breaking to Evolution after a Quench, Phys. Rev. Lett. **109**, 175302 (2012).

[11] U.-J. Wiese, Ultracold quantum gases and lattice systems: Quantum simulation of lattice gauge theories, Ann. Phys. (NY) **525**, 777 (2013).

[12] U.-J. Wiese, Towards quantum simulating QCD, Nucl. Phys. A **931**, 246 (2014).

[13] S. P. Jordan, K. S. M. Lee, and J. Preskill, Quantum algorithms for fermionic quantum field theories, arXiv:1404.7115 [hep-th].

[14] L. García-Álvarez, J. Casanova, A. Mezzacapo, I. L. Egusquiza, L. Lamata, G. Romero, and E. Solano, Fermion-Fermion Scattering in Quantum Field Theory with Superconducting Circuits, Phys. Rev. Lett. **114**, 070502 (2015).

[15] D. Marcos, P. Widmer, E. Rico, M. Hafezi, P. Rabl, U. J. Wiese, and P. Zoller, Two-dimensional lattice gauge theories with superconducting quantum circuits, Ann. Phys. (NY) **351**, 634 (2014).

[16] A. Bazavov, Y. Meurice, S.-W. Tsai, J. Unmuth-Yockey, and J. Zhang, Gauge-invariant implementation of the Abelian Higgs model on optical lattices, Phys. Rev. D **92**, 076003 (2015).

[17] E. Zohar, J. I. Cirac, and B. Reznik, Quantum simulations of lattice gauge theories using ultracold atoms in optical lattices, Rep. Prog. Phys. **79**, 014401 (2016).

[18] A. Mezzacapo, E. Rico, C. Sabín, I. L. Egusquiza, L. Lamata, and E. Solano, Non-Abelian $SU(2)$ Lattice Gauge Theories in Superconducting Circuits, Phys. Rev. Lett. **115**, 240502 (2015).

[19] M. Dalmonte and S. Montangero, Lattice gauge theory simulations in the quantum information era, Contemp. Phys. **57**, 388 (2016).

[20] E. Zohar, A. Farace, B. Reznik, and J. I. Cirac, Digital lattice gauge theories, Phys. Rev. A **95**, 023604 (2017).

[21] E. A. Martinez *et al.*, Real-time dynamics of lattice gauge theories with a few-qubit quantum computer, Nature (London) **534**, 516 (2016).

[22] A. Bermudez, G. Aarts, and M. Müller, Quantum Sensors for the Generating Functional of Interacting Quantum Field Theories, Phys. Rev. X **7**, 041012 (2017).

[23] J. M. Gambetta, J. M. Chow, and M. Steffen, Building logical qubits in a superconducting quantum computing system, npj Quantum Inf. **3**, 2 (2017).

[24] L. Krinner, M. Stewart, A. Pazmiño, J. Kwon, and D. Schneble, Spontaneous emission of matter waves from a tunable open quantum system, Nature (London) **559**, 589 (2018).

[25] A. Macridin, P. Spentzouris, J. Amundson, and R. Harnik, Electron-Phonon Systems on a Universal Quantum Computer, Phys. Rev. Lett. **121**, 110504 (2018).

[26] T. V. Zache, F. Hebenstreit, F. Jendrzejewski, M. K. Oberthaler, J. Berges, and P. Hauke, Quantum simulation of lattice gauge theories using Wilson fermions, Sci. Technol. **3**, 034010 (2018).

[27] J. Zhang, J. Unmuth-Yockey, J. Zeiher, A. Bazavov, S. W. Tsai, and Y. Meurice, Quantum Simulation of the Universal Features of the Polyakov Loop, Phys. Rev. Lett. **121**, 223201 (2018).

[28] N. Klco, E. F. Dumitrescu, A. J. McCaskey, T. D. Morris, R. C. Pooser, M. Sanz, E. Solano, P. Lougovski, and M. J. Savage, Quantum-classical computation of Schwinger model dynamics using quantum computers, Phys. Rev. A **98**, 032331 (2018).

[29] N. Klco and M. J. Savage, Digitization of scalar fields for quantum computing, Phys. Rev. A **99**, 052335 (2019).

[30] H.-H. Lu *et al.*, Simulations of subatomic many-body physics on a quantum frequency processor, Phys. Rev. A **100**, 012320 (2019).

[31] N. Klco and M. J. Savage, Minimally-entangled state preparation of localized wavefunctions on quantum computers, arXiv:1904.10440 [quant-ph].

[32] H. Lamm and S. Lawrence, Simulation of Nonequilibrium Dynamics on a Quantum Computer, Phys. Rev. Lett. **121**, 170501 (2018).

[33] E. Gustafson, Y. Meurice, and J. Unmuth-Yockey, Quantum simulation of scattering in the quantum Ising model, Phys. Rev. D **99**, 094503 (2019).

[34] N. Klco, J. R. Stryker, and M. J. Savage, SU(2) non-Abelian gauge field theory in one dimension on digital quantum computers, Phys. Rev. D **101**, 074512 (2020).

[35] A. Alexandru, P. F. Bedaque, H. Lamm, and S. Lawrence (NuQS Collaboration), σ Models on Quantum Computers, Phys. Rev. Lett. **123**, 090501 (2019).

[36] A. Alexandru, P. F. Bedaque, S. Harmalkar, H. Lamm, S. Lawrence, and N. C. Warrington (NuQS Collaboration), Gluon field digitization for quantum computers, Phys. Rev. D **100**, 114501 (2019).

[37] N. Mueller, A. Tarasov, and R. Venugopalan, Deeply inelastic scattering structure functions on a hybrid quantum computer, arXiv:1908.07051 [hep-th].

[38] H. Lamm, S. Lawrence, and Y. Yamauchi (NuQS Collaboration), Parton physics on a quantum computer, Phys. Rev. Research **2**, 013272 (2020).

[39] G. Magnifico, M. Dalmonte, P. Facchi, S. Pascazio, F. V. Pepe, and E. Ercolessi, Real time dynamics and confinement in the $\mathbb{Z}_n$ Schwinger-Weyl lattice model for 1+1 QED, arXiv:1909.04821 [quant-ph].

[40] B. Chakraborty, M. Honda, T. Izubuchi, Y. Kikuchi, and A. Tomiya, Digital quantum simulation of the Schwinger model with topological term via adiabatic state preparation, arXiv:2001.00485 [hep-lat].

[41] K. Fukushima, D. E. Kharzeev, and H. J. Warringa, The chiral magnetic effect, Phys. Rev. D **78**, 074033 (2008).

[42] D. E. Kharzeev, The chiral magnetic effect and anomaly-induced transport, Prog. Part. Nucl. Phys. **75**, 133 (2014).

[43] D. E. Kharzeev, K. Landsteiner, A. Schmitt, and H.-U. Yee, *Strongly Interacting Matter in Magnetic Fields: A Guide to This Volume* (Springer, Berlin, Heidelberg, 2013), pp. 1–11.

[44] J. S. Bell and R. Jackiw, A PCAC puzzle: $\pi^0 \to \gamma\gamma$ in the σ model, Nuovo Cimento A **60**, 47 (1969).

[45] S. L. Adler, Axial vector vertex in spinor electrodynamics, Phys. Rev. **177**, 2426 (1969).

[46] D. Kharzeev, Parity violation in hot QCD: Why it can happen, and how to look for it, Phys. Lett. B **633**, 260 (2006).

[47] D. E. Kharzeev, J. Liao, S. A. Voloshin, and G. Wang, Chiral magnetic and vortical effects in high-energy nuclear collisions – A status report, Prog. Part. Nucl. Phys. **88**, 1 (2016).

[48] Q. Li, D. E. Kharzeev, C. Zhang, Y. Huang, I. Pletikosic, A. V. Fedorov, R. D. Zhong, J. A. Schneeloch, G. D. Gu, and T. Valla, Chiral magnetic effect in $ZrTe_5$, Nat. Phys. **12**, 550 (2016).

[49] D. E. Kharzeev and H. J. Warringa, Chiral magnetic conductivity, Phys. Rev. D **80**, 034028 (2009).

[50] D. E. Kharzeev and H.-U. Yee, Chiral magnetic wave, Phys. Rev. D **83**, 085007 (2011).

[51] J. S. Schwinger, Gauge invariance and mass. II, Phys. Rev. **128**, 2425 (1962).

[52] S. R. Coleman, R. Jackiw, and L. Susskind, Charge shielding and quark confinement in the massive Schwinger model, Ann. Phys. (NY) **93**, 267 (1975).

[53] S. R. Coleman, More about the massive Schwinger model, Ann. Phys. (NY) **101**, 239 (1976).

[54] N. S. Manton, The Schwinger model and its axial anomaly, Ann. Phys. (NY) **159**, 220 (1985).

[55] T. V. Zache, N. Mueller, J. T. Schneider, F. Jendrzejewski, J. Berges, and P. Hauke, Dynamical Topological Transitions in the Massive Schwinger Model with a θ Term, Phys. Rev. Lett. **122**, 050403 (2019).

[56] A. Casher, J. B. Kogut, and L. Susskind, Vacuum polarization and the absence of free quarks, Phys. Rev. D **10**, 732 (1974).

[57] L. Susskind, Lattice fermions, Phys. Rev. D **16**, 3031 (1977).

[58] P. Jordan and E. P. Wigner, About the Pauli exclusion principle, Z. Phys. **47**, 631 (1928).

[59] P. Weinberg and M. Bukov, QuSpin: a python package for dynamics and exact diagonalisation of quantum many body systems part I: spin chains, SciPost Phys. **2**, 003 (2017).

[60] T. Fujita and J. Hüfner, Quark fragmentation function in the Schwinger model, Phys. Rev. D **40**, 604 (1989).

[61] C. Y. Wong, R.-C. Wang, and C. C. Shih, Study of particle production using two-dimensional bosonized QED, Phys. Rev. D **44**, 257 (1991).

[62] F. Loshaj and D. E. Kharzeev, LPM effect as the origin of the jet fragmentation scaling in heavy ion collisions, Int. J. Mod. Phys. E **21**, 1250088 (2012).

[63] D. E. Kharzeev and F. Loshaj, Jet energy loss and fragmentation in heavy ion collisions, Phys. Rev. D **87**, 077501 (2013).

[64] D. E. Kharzeev and F. Loshaj, Anomalous soft photon production from the induced currents in Dirac sea, Phys. Rev. D **89**, 074053 (2014).

[65] J. Berges, S. Floerchinger, and R. Venugopalan, Dynamics of entanglement in expanding quantum fields, J. High Energy Phys. 04 (2018)145.